

# Color-Selective 2.5D Holograms on Large-Area Flexible Substrates for Sensing and Multilevel Security

Yetisen, Ali K.; Butt, Haider; Mikulchyk, Tatsiana; Ahmed, Rajib; Montelongo, Yunuen; Humar, Matjaž; Jiang, Nan; Martin, Suzanne; Naydenova, Izabela; Yun, Seok Hyun

DOI:

[10.1002/adom.201600162](https://doi.org/10.1002/adom.201600162)

License:

None: All rights reserved

Document Version

Peer reviewed version

Citation for published version (Harvard):

Yetisen, AK, Butt, H, Mikulchyk, T, Ahmed, R, Montelongo, Y, Humar, M, Jiang, N, Martin, S, Naydenova, I & Yun, SH 2016, 'Color-Selective 2.5D Holograms on Large-Area Flexible Substrates for Sensing and Multilevel Security', *Advanced Optical Materials*. <https://doi.org/10.1002/adom.201600162>

[Link to publication on Research at Birmingham portal](#)

## Publisher Rights Statement:

This is the peer reviewed version of the following article: Yetisen, A. K., Butt, H., Mikulchyk, T., Ahmed, R., Montelongo, Y., Humar, M., Jiang, N., Martin, S., Naydenova, I. and Yun, S. H. (2016), Color-Selective 2.5D Holograms on Large-Area Flexible Substrates for Sensing and Multilevel Security. *Advanced Optical Materials*., which has been published in final form at <http://dx.doi.org/10.1002/adom.201600162>. This article may be used for non-commercial purposes in accordance with Wiley Terms and Conditions for Self-Archiving.

Checked 24/8/2016

## General rights

Unless a licence is specified above, all rights (including copyright and moral rights) in this document are retained by the authors and/or the copyright holders. The express permission of the copyright holder must be obtained for any use of this material other than for purposes permitted by law.

- Users may freely distribute the URL that is used to identify this publication.
- Users may download and/or print one copy of the publication from the University of Birmingham research portal for the purpose of private study or non-commercial research.
- User may use extracts from the document in line with the concept of 'fair dealing' under the Copyright, Designs and Patents Act 1988 (?)
- Users may not further distribute the material nor use it for the purposes of commercial gain.

Where a licence is displayed above, please note the terms and conditions of the licence govern your use of this document.

When citing, please reference the published version.

## Take down policy

While the University of Birmingham exercises care and attention in making items available there are rare occasions when an item has been uploaded in error or has been deemed to be commercially or otherwise sensitive.

If you believe that this is the case for this document, please contact [UBIRA@lists.bham.ac.uk](mailto:UBIRA@lists.bham.ac.uk) providing details and we will remove access to the work immediately and investigate.

DOI: 10.1002/

Article type: Full Paper

## Color-Selective 2.5 Dimensional Holograms on Large-Area Flexible Substrates for Sensing and Multilevel Security

*Ali K. Yetisen,\* Haider Butt, Tatsiana Mikulchyk, Rajib Ahmed, Yunuen Montelongo, Matjaž Humar, Nan Jiang, Suzanne Martin, Izabela Naydenova, Seok Hyun Yun\**

Dr. A. K. Yetisen, Dr. M. Humar, Dr. Nan Jiang, Prof. S. H. Yun

Harvard Medical School and Wellman Center for Photomedicine, Massachusetts General Hospital, 65 Landsdowne Street, Cambridge, MA, 02139, USA

Harvard-MIT Division of Health Sciences and Technology, Massachusetts Institute of Technology, Cambridge, MA, 02139, USA

E-mail: ayetisen@mgh.harvard.edu, syun@mgh.harvard.edu

Dr. H. Butt, R. Ahmed

Nanotechnology Laboratory, School of Engineering, University of Birmingham, Birmingham, B15 2TT, UK

Dr. Y. Montelongo

Department of Chemistry, Imperial College London, South Kensington Campus, London SW7 2AZ, UK

T. Mikulchyk, Dr. S. Martin, Dr. I. Naydenova

Centre for Industrial and Engineering Optics, School of Physics, College of Sciences and Health, Dublin Institute of Technology, Kevin Street, Dublin 8, Ireland

Keywords: Holography; photonics; nanosteps; nanoimprinting; Bragg gratings; colorimetric sensing; multilevel security

**ABSTRACT**

2.5D photonic nanostructures with narrow-band diffraction characteristics have a vast range of potential applications in data storage, security, tunable lasers, optical filters, and biosensors. However, fabrication of 2.5D photonic devices over large areas remains expertise-dependent, inaccurate, and high-cost, limiting their widespread use in practical applications and consumer products. Here, we demonstrate large area printing of quasi 2.5D holograms in the visible spectrum. These holographic surface-relief gratings are hexagonally-packed lateral microscale honeycomb pyramids consisting of vertical nanoscale steps. The consecutive steps act as Bragg gratings producing constructive interference of selective visible wavelengths. The 2.5D nanosteped pyramids exhibited a strong coloration due to the narrow-band Bragg diffraction that was tuned in the visible spectrum and a wide angular range. Roll-to-roll processing has allowed rapid printing the 2.5D nanosteped pyramid arrays over large areas of acrylate polymer film on poly(ethylene terephthalate) (PET) substrate. We demonstrate the utilities of the 2.5D holograms by creating a colorimetric refractive index and relative humidity sensors visible to the eye, and multilevel security labels with encrypted information including angular convolution. We envision that 2.5D holograms can be integrated with desktop dot-matrix printers for application in sensors, data storage devices, and security labels.

## 1. Introduction

Photonic nanostructures operating from ultraviolet to near-infrared regions have applications in tunable lasers, light trapping, optical filters, data storage, dynamic displays, and biosensors.<sup>[1, 2]</sup> Photonic structures have been fabricated by self-assembly and microfabrication, or combination of both.<sup>[3]</sup> Bottom-up fabricated periodic optical nanostructures include crystalline colloidal arrays,<sup>[4]</sup> inverse opals,<sup>[5]</sup> block copolymer gratings,<sup>[6]</sup> and Bragg stacks.<sup>[7]</sup> However, photonic structures obtained by self-assembly methods are prone to defects; therefore, the mass production of uniform, defect-free, large-area 3D photonic structures, in particular with narrow-band diffraction in the visible spectrum is limited.<sup>[8]</sup> For example, producing high-quality monodisperse, highly-charged polystyrene particles through emulsion polymerization to prepare opals require lengthy dialysis times (hours to days), limiting their potential for practical applications.<sup>[1]</sup> Other self-assembly approaches including layer-by-layer deposition and spin coating suffer from layer instability and time-consuming fabrication processes. Top-down approaches such as electron beam lithography,<sup>[9]</sup> focused ion beam milling,<sup>[10]</sup> multi-directional etching<sup>[11]</sup> and laser lithography<sup>[12]</sup> of single-crystalline semiconductors or dielectric materials allow direct creation of high-quality 3D photonic structures. Silicon, gallium arsenide, and tungsten have been incorporated into 3D templates *via* chemical vapor deposition, followed by removal at a later stage.<sup>[13]</sup> Direct fabrication of 3D PCs was also demonstrated through layer-by-layer assembly involving multiple lithographic writing and etching steps.<sup>[14]</sup> However, these approaches require wafer fusion for each layer and accurate alignment of the setup. Furthermore, 3D photonic crystal woodpile structures with a complete gap of 3.5% have been fabricated by direct laser writing in chalcogenide glasses in 2 h.<sup>[12]</sup> 3D photonic nanostructures operating at near-infrared and longer wavelengths larger than  $100\text{ }\mu\text{m} \times 100\text{ }\mu\text{m} \times 100\text{ }\mu\text{m}$  with uniformity have been fabricated *via* laser lithography.<sup>[15]</sup> However, these

3D nanostructures typically have periodicities of the order of several microns that display photonic bandgaps beyond the visible range. Additionally, 3D structures cannot be mass produced through embossing or roll-to-roll printing. 2.5D photonic structures have also emerged as a major extension of 2D planar semiconductor technologies with an added third vertical dimension using multilayer stacks.<sup>[16]</sup> Hence, in 2.5D photonic structures, lateral index contrast is combined with a 1D vertical high-index contrast.<sup>[17]</sup> Analogous to their 3D counterparts, 2.5D are fabricated by molecular beam epitaxy, chemical vapor deposition, electron beam lithography, wet chemical etching, and wafer bonding.<sup>[18]</sup> Therefore, a technique to accurately print color-selective 2.5D photonic nanostructures on flexible substrates in a single step at industrial production speeds is desirable.

Denisyuk's work on reflection holograms in the 1960s has led to imaging 3D objects using laser light.<sup>[19]</sup> Denisyuk holography involves recording a latent image of scattered light from an object in a light-sensitive recording medium *via* silver halide chemistry or dichromated gelatin.<sup>[20]</sup> The recorded latent image can be amplified by photographic developers or application of heat. When illuminated with a broad-band light, reflection holograms diffract narrow-band (monochromatic) light.<sup>[21]</sup> The lattice spacing and the Bragg peak of the diffracted light can be controlled by changing the wavelength of laser light that was used to record the hologram or swelling/shrinking the recording medium to create pseudocolors.<sup>[22]</sup> These structures cannot be multiplied by embossing. Holography can also be configured to operate in transmission mode to image 3D objects. This method, known as off-axis Leith-Upatnieks holography, requires a monochromatic light source to replay recorded image.<sup>[23]</sup> Gratings recorded in photoresist films can be used to produce a metal master hologram that can be embossed on a surface.<sup>[24]</sup> These gratings, known as Benton holograms, diffract rainbow colors when illuminated with broadband light.

Here, we demonstrate the development and optical characterization of large area printing of quasi 2.5D photonic structures in the visible spectrum and show their application in sensors

and displays. These structures are hexagonally-packed lateral microscale pyramids consisting of vertical nanoscale steps. The consecutive steps act as Bragg gratings producing constructive interference of selective visible wavelengths. In our strategy, we combine prism coupling interference and off-axis Leith-Upatnieks holography to create printable 2.5D photonic nanostructures. Analogous to volume holograms, the present technology also provides tunability of the diffraction in the visible spectrum. The present work demonstrates open 2.5D surface relief patterns to print Bragg gratings. This strategy allows efficient printing of uniform, defect-free color-selective 2.5D photonic structures that feature improved versatility and scalability at low cost. We printed these photonic structures on flexible polymer substrates in roll-to-roll manufacturing with industrial scalability. We show the utilities of the 2.5D structures by creating colorimetric refractive index and relative humidity sensors, and multilevel security labels with encrypted information and angular convolution.

## 2. Results and Discussion

### 2.1. Design and Optimization of the Photonic Structures

The 2.5D photonic structures comprise of a honeycomb array with circular convex step-variable gratings, resembling Teuchitlan pyramids (Guachimontones, Mexico) (**Figure 1a**). These structures show narrow-band colors produced as a result of stepped structures.<sup>[25]</sup> The hexagonal array of circular hollow pyramids was designed to have a pitch of 3.3  $\mu\text{m}$  and an apex-base distance of  $\sim 1.1 \mu\text{m}$ . The pyramids consist of 5-6 nanosteps, with a variable step height ( $h$ ) from 160 ( $h_1$ ) to 200 nm ( $h_2$ ), and a step width of 250 nm. The pyramids are made of acrylate polymer (AP) ( $n \approx 1.49$ ) on poly(ethylene terephthalate) (PET) film ( $n \approx 1.57$ ), and their inner surface has an aluminum coating (20 nm,  $\underline{n} = 1.09 + i6.79$ ). Prior to fabrication, the optical properties of thin layer of the honeycomb array of nanosteped pyramids were analyzed by computational modeling. The interaction of the electromagnetic field with the nanosteped pyramids was modeled within a hemisphere screen using COMSOL

Multiphysics by using finite **element method** (Figure 1b). Methods ‘Modeling of the Honeycomb Nanosteped Pyramids’ describes the parameters of the model. The light wave propagation at a normal incidence was **computed** for nanosteped pyramids with different step sizes ranging from 160 to 200 nm. Figure 1c-e illustrates the electromagnetic field distributions within the hemisphere screen for the modeled geometries with step heights of 160, 180, and 200 nm while keeping the step width constant at 250 nm.

The blue resonance of the diffracted light (496 nm) is focused near zero order (Figure 1c), whereas for red resonance (612 nm), the diffracted light diverges from the zero order (Figure 1e). As the step height increased from 160 to 200 nm; the central wavelength of the narrow-band reflected light shifted from 496 to 612 nm (Figure 1f). Thus, varying the step height allowed tuning the color of the grating throughout the visible spectrum. Bragg peak was narrowband due to the periodicity in the vertical direction. The shift in the position of the Bragg peak with increasing step height had a linear trend (Figure 1g). The full width at half maximum (FWHM) of the simulated structures broadened from 38 to 74 nm with increasing step height as the total height of the pyramids was kept constant (Figure 1g inset).

Additionally, the diffraction efficiency of the Bragg peak could be controlled by changing the number of steps in the pyramids. The reflection of the gratings increased from 40 % to 95 % as the number of steps increased from 4 to 12 (Figure 1h). The inset in Figure 1h shows the enhancement in the reflection of the simulated spectra for 4, 8, and 12 steps, and bandwidth narrowing with increasing step number.

## 2.2. Laser Writing of Holographic 2.5D Nanostructures

The photonic nanosteped pyramids were fabricated by multibeam holographic lithography and subsequently nanoimprinted with AP on PET film. The pyramidal pattern was obtained by superposing multilayer and honeycomb exposure fields in a positive photoresist layer (diazonaphthoquinone, thickness=1.2  $\mu\text{m}$ ,  $n=1.65$ ). First, the holographic interference pattern

coplanar with the photoresist surface ( $\varnothing=14$  cm) was photochemically patterned using prism coupling (**Figure 2a**). To obtain a multilayer exposure, a triangular gadolinium gallium garnet prism ( $n=1.97$ ) was aligned over the photoresist layer, where the refractive index was matched by xylene ( $n=1.49$ ). The total internal reflection of a coherent argon ion laser beam ( $\lambda=458$  nm, 100 mW) from the photoresist-air interface for 1 min created the multilayer interference pattern. By increasing the angle of incidence normal at the prism surface plane from  $30^\circ$  to  $44^\circ$ , the vertical lattice step height of the multilayer pattern was tuned from 160 to 200 nm at different regions of the photoresist. To create hexagonally packed cylindrical interference fringes running normal to the photoresist surface plane, three azimuthal beams ( $\alpha=120^\circ$ ) were interfered in the photoresist layer to create a pitch ( $w$ ) of  $3.3\ \mu\text{m}$  (**Figure 2b**). The resulting structure is a superposition of a multilayer interference and a hexagonally-packed interference pattern consisting of circular concavities (**Figure 2c**). After the photographic development of the photoresist, the intensity variations are translated into nanosteppped pyramids (**Figure 2d**). ‘Holographic Recording of the Honeycomb Nanosteppped Concavities’ in the Methods demonstrates step-by-step fabrication of the devices.

To print the 2.5D photonic structure on flexible substrates, an inverse master was produced. A silver layer (300 nm) was deposited over the photoresist to form a conductive layer (**Figure 2e**), thus allowing electroplating of metallic nickel over the concavities (**Figure 2f**). The nickel master ( $14\times 14\ \text{cm}^2$ ,  $t=1$  mm) consisting of convex stepped pyramids was installed onto a cylindrical drum of a roller-type replication machine, and the AP pyramids were nanoimprinted onto a PET film (50  $\mu\text{m}$ ) (**Figure 2g**).<sup>[26, 27]</sup> The inset in **Figure 2g** shows the imprinted film consisting of stripes with different nanostep heights in the visible spectrum. To increase the diffraction efficiency, an aluminium layer (20 nm) was coated over the concavities. AP nanosteppped pyramids were printed over  $1\ \text{m}^2$  of PET film within a minute *via* roll-to-roll manufacturing, allowing a scalable production of gratings on large surface areas. The resulting structures were instantaneously usable as narrow-band Bragg gratings



with peaks spanning the visible spectrum, depending on the experimental parameters used to create the nickel master. The step-by-step fabrication is described in the Methods ‘Printing Bragg Gratings in Roll-to-Roll Manufacturing’.

To predict the interference patterns which produce the multilayer and the honeycomb pattern in the photoresist, laser light interference arising from superposition of multiple light waves was modeled. The creation of the nanostructure was simulated for multilayer interference in prism coupling, and off-axis Leith-Upatnieks interference.<sup>[28]</sup> We evaluated the interference pattern created by two main waves: (1) the incident beam to the photoresist, and (2) the beam reflected internally at the photoresist-substrate-air interface during prism coupling exposure. Figure 2h shows the lattice spacing of the multilayer as a function of incident angle in prism coupling. The vertical lattice spacing (height) is:

$$h = \frac{\lambda}{2n \cos \theta} \quad (1)$$

where  $\lambda$  is the wavelength of the laser light,  $n$  is the refractive index of the photoresist, and  $\theta$  is the incident angle measured with respect to the normal to the prism surface plane. Equation (1) shows the principle of prism coupling holographic recording, obeying Bragg’s law.

Increasing  $\theta$  from  $10^\circ$  to  $60^\circ$  allows tuning the step height from 150 to 275 nm. The off-axis Leith-Upatnieks interference was modeled by calculating the superposition of three azimuthal beams. To retrieve the honeycomb exposure, the interference of three wave fronts was computed:

$$E_1(r, t) = Ae^{i\left(\frac{2\pi n}{\lambda}(x\sin(\alpha)+z\cos(\alpha))-\omega t+\phi_1\right)} \quad (2)$$

$$E_2(r, t) = Ae^{i\left(\frac{2\pi n}{\lambda}\left(\frac{-x\sin(\alpha)}{2}+\frac{y\sqrt{3}\cos(\alpha)}{2}+z\cos(\alpha)\right)-\omega t+\phi_2\right)} \quad (3)$$

$$E_3(r, t) = Ae^{i\left(\frac{2\pi n}{\lambda}\left(\frac{-x\sin(\alpha)}{2}-\frac{y\sqrt{3}\cos(\alpha)}{2}+z\cos(\alpha)\right)-\omega t+\phi_3\right)} \quad (4)$$

where  $E(r, t)$  is the electric vector,  $A$  is the wave amplitude,  $\omega$  is the angular frequency, and  $\phi$  is the phase of the plane waves. The three wave vectors are defined with a polar angle from

the normal  $\alpha$  and azimuthal angles of  $0^\circ$ ,  $120^\circ$ , and  $240^\circ$ . The waves constructively and destructively interfere in the photoresist producing an intensity distribution:

$$\langle I(r) \rangle = \int_0^t |E_1(r, t) + E_2(r, t) + E_3(r, t)|^2 dt \propto |E_1(r) + E_2(r) + E_3(r)|^2 \quad (5)$$

To visualize the intensity distribution at the surface plane of the photoresist, the electromagnetic field in every point over  $10 \times 10 \mu\text{m}^2$  in the photoresist was evaluated. Through computing the respective intensities and phases of individual plane waves, an interference pattern was extracted (Figure 2i). White (high intensity) and black regions represent the spatial variation of light intensity for the photoresist exposure. This exposure creates a honeycomb interference pattern that runs perpendicular to the surface plane of the photoresist. Superposing the multilayer interference and the off-axis Leith-Upatnieks interference produces a circular nanostep pyramid. Figure 2j shows the 3D intensity distribution of the superposed fields in the photoresist, where the pitch of the honeycomb is  $3.3 \mu\text{m}$ , and the depth of a nanostep pyramid is  $1.1 \mu\text{m}$ .

### 2.3. Microscopic analyses of the holographic nanosteps

**Figure 3a** illustrates scanning electron microscope (SEM) images of a honeycomb array produced with an incident angle  $\theta$  of  $40^\circ$  during prism coupling (Methods ‘SEM Protocol’). The inset in Figure 3a shows a single concavity with 6 steps. The SEM images of the vertical cross-section of the sample show that circular concavities have uniform step profiles (Figure 3b). The number of steps of the concavities decreased from 6 to 5 as the incident angle  $\theta$  was increased from  $30^\circ$  to  $44^\circ$  during prism coupling. Figure 3c shows atomic force microscope (AFM) 3D surface topography of the honeycomb array within  $5 \times 5 \times 2 \mu\text{m}^3$  (Methods ‘AFM Protocol’). Figure S1 shows reproducibility of the array at large dimensions. The pitch of the concavities in the honeycomb array was  $3.3 \mu\text{m}$ , and a single concavity had a step height ranging from  $\sim 160$  to  $\sim 200$  nm, respectively (Figure 3d). The step width was  $\sim 250$  nm in all

samples. As supported by the experimental measurements, the concavity distribution and the surface topography of the structures can be accurately predicted by prism coupling and off-axis Leith-Upatnieks interference models (equation (1-5)).

## 2.4. Optical Characterization of Holographic Nanostructures

**Figure 4a** shows the photographs of the honeycomb array viewed from normal to the PET side. Changing the incident angle from  $30^\circ$  to  $44^\circ$  with  $2^\circ$  increments during prism coupling increased the step height of the pyramids from 160 to 200 nm. This tuning mechanism allows shifting the diffracted light by 2.8 nm/deg in the entire visible spectrum. The nanosteped pyramids were illuminated vertically by a laser beam ( $\lambda=532$  nm) and a fiber optic diffuse broadband light source, and the back scattered light was projected on the screen of a semitransparent hemisphere screen. Under monochromatic illumination, the array diffracted multiple orders in hexagonal spots (Figure 4b). The 1<sup>st</sup>, 2<sup>nd</sup>, 3<sup>rd</sup> and 4<sup>th</sup> diffracted orders were measured at approximately  $10^\circ$ ,  $21^\circ$ ,  $30^\circ$ , and  $40^\circ$  due to the periodicity of the hexagonal pattern. Figure 4c-e shows the diffracted light from three different honeycomb arrays with nanosteped pyramids comprising step heights of 160, 180, and 200 nm, respectively. Under illumination with diffused incident light, the photonic structure diffracts light over the hemisphere screen up to  $20^\circ$  from the normal. Additionally, the grating diffracts violet light at angles higher than  $20^\circ$  under diffuse light illumination.

The spectra of the Bragg peaks were measured using an optical fiber coupled into a port of an upright optical microscope. The Bragg peaks of the nanosteped pyramids with step heights ranging from 160 to 200 nm were measured at normal incidence. Figure 4f shows the photonic band gaps of the pyramids with the step heights of 160, 180, 200 nm, blue, green and red lines, respectively. The spectral bandwidths of the Bragg peaks increased as the step height increased from 160 to 200 nm. The bandwidths were approximately equal to the reciprocal of the number of steps. Figure S2 shows Bragg peaks of eight different arrays. To

measure the diffraction efficiency, the nanosteped pyramids were illuminated approximately normal to the surface plane either with 491, 532, 640 nm laser beams. The diffracted light from individual diffraction spots were measured with an optical power meter. The maximum diffraction efficiency was calculated by adding the diffraction efficiencies of the first three orders in the hexagonal pattern. When illuminated with 491, 532, and 650 nm light, gratings with step sizes of 160, 180, and 200 nm had the maximum efficiencies of 15.5 %, 10.6 %, and 6.8%, respectively. The decrease in the diffraction efficiency with increasing step height can be attributed to the decreased in the number of steps. Figure S3 shows the first order reflective diffraction efficiencies of the nanosteped pyramids. To resolve the angular diffraction, a 3 mm spot on the stepped pyramids was illuminated at normal incidence with a broad-band light source. The backscattered light was spectrally analyzed at 1° increments from 0° to 60° relative to the sample normal using a spectrometer positioned on a robotic goniometer. Figure 4g illustrates the angle-resolved spectra of pyramids with step height of 190 nm for different collection angles as a function of diffraction intensity. The normal incidence Bragg peak at 530 nm (indicated by an arrow in Figure 4g) was visible in all of the higher-order diffraction modes following an arc-shaped pattern as predicted by Bragg's law for changing incidence angle. The Bragg grating diffracted narrow-band light at ~10° from normal with an efficiency of 1.4 % measured for a single 1<sup>st</sup> order diffraction spot in the blue/green region (~520 nm). The nanosteped pyramids Bragg-diffracted the light analogous to a multilayer reflection grating. Figure 4g shows the diffraction angle; the coherent scattering of the Bragg multilayer peak and a surface grating are superposed to create a hierarchical optical characteristic of the photonic structure. There were also minor increases in the intensity of non-Bragg regions. This feature could be caused by the parabolic nature of the concavity depressions, variation in step height or thickness of the sample. The parabolic depression profile of the step height may be attributed to the nonlinear etching of photoresist due to the decrease in the concentration of developer or desensitization of the surface. Figure 4h illustrates the zero and first order Bragg

peak positions as a function of step height. As the step height was increased from 160 to 200 nm, the zero and first order Bragg peaks red shifted by 120 and 100 nm, respectively. The direction of the first diffracted light was  $\sim 10^\circ$  from the normal (Figure 4h inset). ‘Optical Characterization’ in the Methods describes measurement devices and techniques.

## 2.5. Refractive Index Sensing

To demonstrate the utility of the nanosteped pyramids, we show an application in sensing. The Bragg peak of the diffracted light from the nanosteped pyramids is affected by changes in the refractive index of the surrounding medium. This feature can be used as a colorimetric refractive index sensor to quantify the concentration of analytes. Finite element method simulations show that as the refractive index of the surrounding medium was increased from 1.33 to 1.47, the Bragg peak shifted from 493 to 532 nm, respectively (**Figure 5a**). Figure S4a illustrates Bragg peaks for eight different simulated refractive index values. Glycerol was utilized as a model sensing analyte. Glycerol is a caloric macronutrient, and its measurement water has applications in pharmaceuticals and food industry. As the surrounding medium of the grating was incrementally changed from deionized water to increasing concentrations of glycerol, the Bragg peak shifted from 495 to 535 nm in the visible spectrum (Figure 5b). **In contrast to the simulated spectra in Figure 5a, the experimental Bragg peak response exhibited negligible side lobes as the number of nanosteped pyramids was significantly higher than the simulated structure.** The Bragg peak followed a linear shift as the concentration of glycerol was increased from 10 to 100 vol % corresponding to a refractive index change from 1.346 to 1.472, respectively (Figure 5c). The experimental readouts agree with a handheld refractometer and simulated Bragg peaks, allowing the prediction of the refractive index of glycerol using computational modeling. The sensitivity of the sensor was 0.00104 refractive index units ( $R^2 = 0.99$ ) corresponding to a concentration of 0.75 (vol %) using a spectrophotometer with 0.3 nm resolution. The sensitivity of the sensor improves with

increasing spectrophotometer resolution. The colorimetric results were visible to the eye within seconds of changing the concentration of the glycerol (Figure 5d). The sensors showed inter-assay reproducibility from batch to batch ( $n=10$ ), and no hysteresis and Bragg peak broadening were recorded; hence, the same sensor can be used for repeat measurements. Recently, aluminum nanoclusters with plasmonic Fano resonances,<sup>[29]</sup> 2D silicon nanowire arrays,<sup>[30]</sup> and porous mixed metal oxide-TiO<sub>2</sub> 1D photonic crystals<sup>[31]</sup> have been reported for colorimetric refractive index sensing. In addition to the comparable sensitivity with the reported sensors, the present holographic technology has the added advantages of easy colorimetric tunability, wide field of view of the diffraction pattern visible to the eye, and rapid imprinting of uniform and low-cost sensors.

## 2.6. Relative humidity sensing

Development of sensors for visual indication of relative humidity (RH) in the environment is essential in industrial and domestic applications. The range of RH that is of interest for any specific application is different; thus, the sensitivity of the sensor needs to be optimized. To demonstrate the flexibility with which the initial appearance and the sensitivity of the nanoimprinted pyramidal structure to an analyte can be changed, a series of experiments were carried out. First, nanosteped pyramidal arrays with step size of 165, 180 and 195 nm were spin-coated with a poly(vinyl alcohol) (PVA) layer. The coating layer suppresses the diffraction from the low spatial frequency periodical structure ( $\sim 3.3 \mu\text{m}$ ) and narrow-band diffraction was observed for different heights of the pyramidal steps (Figure 5e). The uncoated honeycomb array diffracted light due to the co-existence of two periodical structures created in holographic reflection and transmission modes. When the photonic structure was coated with a PVA layer, the refractive index modulation responsible for the diffraction from the transmission structure significantly decreased. Initially, the refractive index modulation was determined by the difference in the refractive indexes of air and the plastic substrate

coated with an aluminium layer ( $\sim 20\text{ }\mu\text{m}$ ). Spin-coating the nanosteps with PVA displaced the air and matched the surrounding refractive index close to the one of the plastic substrate. Thus, the efficiency of the transmission grating was diminished and the optical response of the device was predominantly determined by the nanosteps. This observation was consistent with the color of the diffracted light that depended on the nanostep height (Figure 5e).

The sensitivity of the sensor was optimized by changing the chemical composition of the coating layer. Aluminum side of the nanosteped pyramidal arrays with a step height of 175 nm were each coated with PVA/Glycerol (1:0, 1:1, 2:3, wt%). The samples were placed in a controlled humidity chamber and were illuminated with a broad spectral range beam of light. Figure 5f shows the dependence of the peak wavelength of the diffracted light on the RH in the chamber. The addition of glycerol to the PVA solution spin-coated on top of the nanosteped pyramidal array structure increases the sensitivity of the sensor – particularly at the low RH range. The repeatability and the reversibility of the changes in devices coated with PVA and PVA/Glycerol (1:1) layers were confirmed after exposure to RH above 90% (Figure 5g). The layer with composition of PVA/Glycerol (2:3) is suitable for operation at lower RH. The presented RH sensors can be explored to create sensors operating at low RH region where the demand for highly sensitive devices in electronics, food and pharmaceutical packaging is high.

## 2.7. Multilevel security labels

We also demonstrate the application of the holographic honeycomb nanosteped pyramids in printing multilevel security labels. Current standard for security labels is surface holograms, which diffract rainbow colors upon illumination with broadband light. Although volumetric 3D holograms can be created through silver halide chemistry or photopolymers (*e.g.*, Polaroid DMP-128), they do not meet cost requirements at high volume. Fake labels or patterns can be easily created to resemble genuine labels, and existing rainbow holograms offer limited

protection against counterfeit products. For example, many reflective materials including silver foil copies, and a convincing fake holograms have been found on counterfeit medicines, which increase about 25% each year.<sup>[32]</sup> Currently, there is a need to produce technically advanced verification mechanisms to prevent counterfeit medicines and other products. To create multilayer security labels, we selectively patterned honeycomb arrays using a photomask to obtain Bragg gratings with step heights of 160, 180, 195, and 200 nm that diffract light at 500, 544, 599, and 620 nm, respectively (Methods ‘Device Assembly’).

**Figure 6a** illustrates an image of the dove used in credit cards. The photonic color-selective capability of the 2.5D nanostructures can be utilized in the identification of counterfeit credit cards. We also printed the nanosteped pyramids as optically encrypted QR codes to securely identify high-volume products for application in drug packages, blister cards, and capsules (Figure 6b). 2.5D nanosteped pyramids can be used in dactyloscopy to biometrically identify an individual, or placed on highly secure documents such as passports, identification documents, and polymer banknotes. For example, the holographic nanosteped pyramids can be used to print pre-scanned fingerprints (Figure 6c). Human fingerprints are unique markers that are difficult to alter, and durable over the life of an individual. Figure 6d shows a handwritten signature for application in personalizing and authenticating autographs. The honeycomb nanosteped pyramids can be visually distinguished from rainbow (polychromatic) holograms and the reflective materials since the present technology provides multilevel authentication of a product: (i) Color-selective diffraction is easily verified; (ii) the array projects a far-field honeycomb pattern when illuminated with laser light, and (iii) the QR code can be decoded easily using a smartphone to rapidly authenticate a product.

Different patterns can be obtained at the far field by using two holograms with a relative angle between them. According to the convolution theorem, the effect observed at the far-field corresponds to the circular convolution of the two independent rotated holograms. This phenomenon can be observed when the holograms work in transmission mode. We have



demonstrated this effect by superposing the two nanosteped pyramidal array holograms with a relative angle between them (Figure 6e). When the angle is zero, the auto-correlation of the hexagonal pattern is equivalent to another hexagonal pattern producing no observable effect of the convolution. However, when the second hologram is rotated, multiple diffractive spots emerging from the hexagonal pattern spots. Furthermore, these spots overlap at larger angle creating complex diffractive patterns. Figure 6f shows far-field images as Hologram 2 was rotated from its original position to  $180^\circ$ , showing distinct diffraction features (field distribution). This effect can be expanded indefinitely by superposing multiple rotated hologram. This technology acts as a secure code analogous to space division multiplexing in the data communication systems. The presented technology can be combined with metasurface holograms with polarization functionalities, plasmonics, or graphene oxide gratings to ensure multilevel security.

## CONCLUSIONS

We developed a top-down strategy to print holographic honeycomb arrays consisting of 2.5D nanosteped pyramids on flexible substrates. Our approach has many attractive attributes due to its exceptional flexibility for tuning the Bragg diffraction of the gratings, possibilities of customization for personal use, and compatibility with mass manufacturing. Predicted by the analytical models for modulating the incident angle ( $\theta$ ) during prism coupling and azimuthal angle ( $\alpha$ ) during off-axis interference, our fabrication approach allows fine-tuning the optical characteristics of the gratings such as the position and the bandwidth of Bragg peak as well as its diffraction intensity based on the accurate modulation of the geometry of the pyramids and the density of hexagonal packing. These 2.5D photonic structures can be printed on flexible substrates to have color-selectivity controlled in the visible spectrum and observed in an angular range of  $20^\circ$  from the normal. We also demonstrated the scalability of this technique by printing the nanosteped pyramids over large

areas ( $1 \text{ m}^2$ ) in roll-to-roll manufacturing within a minute. The application of the nanosteppped pyramids was demonstrated in quantitatively sensing refractive index. Our production strategy allows using a large variety of materials as film substrates, including transparent and opaque hydrophobic or hydrophilic polymers, with simple or complex geometries. Furthermore, using our technique, 2.5D nanosteppped pyramids can be selectively patterned and multiplexed within a single device. Such information may be kept as proprietary information and used for the secure verification of high-value products and legal documents.

The ability to produce nanoscale color-selective gratings with large area on flexible substrate has broad applications. For example, these materials may find applications in solar cells, optical devices, tissue engineering, imaging, or photomedicine. In optics, they can be patterned as Fresnel lenses to focus monochromatic light in solar panels. Furthermore, they can be integrated with actuators based on electronics, heating, magnetism, or acoustics to tune the wavelength of the Bragg peak. These mechanisms may allow creating tunable lasers. The surface of nanosteppped pyramids can be functionalized with analyte-sensitive hydrogels to be selective to biomolecules such as pH, metal ions, glucose, proteins, and DNA.<sup>[33]</sup> The color of the diffracted light might be read to quantify the concentration of these analytes for application in microfluidic point-of-care diagnostics. For applications in tissue engineering, the nanosteppped gratings can be used with hydrogels to map localized metabolite changes in scaffolds. Since these gratings can be miniaturized they might be integrated in fiber optics and waveguides for application in biomedical imaging techniques and photodynamic therapy.<sup>[34]</sup> We envision that 2.5D holographic honeycomb nanosteppped pyramids can be integrated with desktop dot-matrix printers.

## Experimental Section

**Electromagnetic modeling of nanosteps.** The diffraction from the gratings was modeled using a finite element method based computational software, COMSOL Multiphysics. The

model consisted of a 2D geometry of nanosteped pyramids with spacing on the order of 3  $\mu\text{m}$ . The 2D simulated geometry represents the cross-section of the 2D pyramid array, taking advantage of the planar symmetry in the x-y plane. The pyramids were made from acrylate polymer (AP) ( $n=1.49$ ) coated with a 30 nm layer of aluminium on poly(ethylene terephthalate) (PET) ( $n=1.57$ ). The unit cell of the geometry consisted of two pyramids with periodic conditions placed across the edges. A hemispherical domain was placed on top of the grating layer, and the area within the hemisphere was defined as air. A broadband light source illuminated the grating normally from the top. The diffracted light was collected from the entrance of the light incident beam.

**Holographic writing of nanostructures.** The samples were fabricated and provided by James J. Cowan (Aztec Systems, Inc., Lexington, MA) and W. Dennis Slafer (MicroContinuum, Inc., Cambridge, MA). The fabrication of the grating consisted of spin coating positive photoresist (diazonaphthoquinone) over a glass substrate (1.0 mm) at 100 rpm for 2 min. The photoresist was baked at 80 °C for 1 h, and it was patterned in two main steps: multilayer exposure (prism coupling) and opening exposure. First, 1/8 of the photoresist surface area, corresponding to a 1.5 cm wide stripe was left open and the rest of the photoresist was blocked with an opaque mask. Xylene ( $n \sim 1.50$ , 1 mL) was deposited over the glass substrate, and a triangular prism was placed over the glass substrate to match the refractive indexes. The contact was between the glass surface of the prism and the glass side of the photoresist coated plate. The photoresist side of this plate is exposed directly to air. In prism coupling, a laser beam ( $\lambda=458$  nm, 100 mW,  $\varnothing=14$  cm) deviated from a mirror mounted on top of an air bearing was scanned over the stripe at 10° from the normal of the prism surface plane for 1 min. This exposure step created a multilayer interference pattern due to total internal reflection in the photoresist-air interface. After the first exposure, the adjacent stripe region was opened and the other regions were masked, and the exposure was carried out at an incident angle of 16° from the normal of the prism surface plane. This process was

repeated until the entire photoresist surface was exposed up to  $50^\circ$  incident beam. The last stripe was used as a blank control. In the second opening exposure step, the entire area of the photoresist layer from the  $\text{SiO}_2$  side was exposed to three azimuthal beams ( $120^\circ$ ) ( $\lambda=458$  nm, 100 mW,  $\varnothing=14$  cm) for 1 min. This process results in hexagonally packed cylindrical interference fringes running normal to the photoresist surface plane. The photoresist was etched using a photographic developer.

**Nanoimprint lithography.** To print the gratings, a master (inverse pattern) originally developed by James J. Cowan (Aztec Systems, Inc.) was used.<sup>[27]</sup> The master protected the original photoresist by creating many working copies. A silver layer ( $\sim 300$  nm) was evaporated over the photoresist in vacuum. The master was fabricated by electroplating metallic nickel over the patterned photoresist in a galvanic tank. The nickel master ( $t=1$  mm) consisted of convex stepped structures extruded from its surface plane. The nickel master was installed onto a cylindrical drum of a roller-type replication machine, and the grating was printed onto AP film ( $\sim 2$   $\mu\text{m}$ ) on a PET substrate ( $\sim 100$   $\mu\text{m}$ ) using UV-initiated nanoimprint lithography. The intensity of UV over the nickel master for curing the acrylate monomer solution on the PET substrate was  $\sim 100$   $\text{mW cm}^{-2}$ , where the web speed was  $20$   $\text{mm s}^{-1}$ . To increase the diffraction efficiency of the convexities, an aluminium layer ( $\sim 20$   $\mu\text{m}$ ) was coated by evaporation over the embossed AP film.

**Scanning electron microscopy.** Gratings from the aluminized AP-PET layer were cut to  $2 \times 2$  mm size. The samples were mounted on a SEM aluminum stub. To image the concavities, Merlin (Zeiss) SEM was used at 1.5 kV with a working distance of 4.1 (cross section) - 5.5 mm (flat) coupled to Signal A: SE2 or InLens detector. Cross sectional images were acquired from the surface plane of the gratings ( $90^\circ$  sample holder).

**Atomic force microscopy.** AFM images were acquired using Cypher AFM (Asylum Research) in AC/tapping mode using an arrow UHF silicon probe (NanoWorld, Asylum Research).

**Nanostructure assembly.** Black opaque masks were printed on a cellulose acetate transparency film (Staples, 21.6×27.9 cm, t=0.1 mm) using a laserjet printer (HP, CP2025). Image colors were inversed before printing. The masks were assembled on the AP side of the gratings. Masks could be used to block light during laser exposure, or the patterns can also be created using CO<sub>2</sub> laser cutting.

**Optical characterization.** The gratings were cut to 1×1 cm<sup>2</sup> square samples and assembled on a robotic rotation mount (Thorlabs) with 360° continuous rotation. A 3 mm spot on the PET surface of the gratings was illuminated at normal incidence with an ultraviolet-visible-near infrared light source (Ocean Optics, DH-2000). The back-scattered spectra was collected at 1° increments from 0° to 60° relative to the sample normal using a reflection spectrometer (Ocean Optics, Maya Pro-2000) positioned on a robotic goniometer controlled by IGOR Pro (v6.3, Wavemetrics). The spectra of the incident light (blank) was recorded by reflecting it from a plane mirror and the diffraction spectra was divided by blank spectra. The intensities of the resulting spectra were normalized to 1.0.

The spectra of the Bragg peaks were measured using an optical fiber coupled into a port of an upright optical microscope (Olympus). Broadband light was used to illuminate the PET side of the gratings normal to the surface plane, and the backscatter was collected from the illumination direction. The spectra of the incident light (blank) was recorded, and the diffraction spectra was divided by blank spectra. The intensities of the resulting spectra were normalized to 1.0.

The hemisphere was fabricated by cutting a semitransparent white plastic ball (Ø=4 cm) in two halves and drilling a 3 mm hole on top of the hemisphere. The gratings from the PET surface side were illuminated normally with an optical fiber (Thorlabs, M13L01 - Ø400 µm, 0.39 NA, 1 m) connected to NCL 150 (Volpi, 20V/150W) broadband cold light halogen lamp. Monochromatic illumination of the gratings was achieved using a continuous wave laser pointer (λ=532 nm, 1 mW, spot Ø=1 mm). Photographs of the gratings from the PET surface

side were captured by a digital single-lens reflex camera (Nikon D90, 12.3 MP) using a Nikkor lens (Nikon, AF-S DX 18-105mm f/3.5-5.6G ED VR).

Diffraction efficiency measurements were carried out by normally illuminating the gratings with a green-blue laser (Cobolt Dual Calypso, Class 3B, 491/532 nm, 100 mW) and red laser (Coherent Cube, 640 nm, 40 mW). The diffracted light was measured both in reflection and transmission modes using a powermeter (Newport, 1918-R). Far-field diffraction measurements of angularly convoluted gratings without Al coating were carried out using a rotation mount. The stationary hologram was fixed on one side of the mount and the other hologram was assembled on the rotating side. The hologram was illuminated with laser light ( $\lambda=532$  nm, 1 mW). A black screen 15 cm away from the rotating hologram was used to project the far-field diffracted light.

**Refractive Index Sensing.** Glycerol stock solutions were prepared from 10 to 90 vol% in water. The glycerol sample (100  $\mu$ L) was deposited over gratings (1 cm<sup>2</sup>) and a cover slip was placed on top. The diffracted light was collected using an upright optical microscope. New gratings were used for each measurement.

**Relative Humidity Sensing.** Nanosteped pyramidal structures with a step height of 175 nm were spin coated with different solutions containing PVA/Glycerol in different ratios (1:0, 1:1, 2:3 wt%). The structures were studied in a controlled humidity and temperature environment (Electro-tech Systems, Inc. Model 5503-11). The RH in the chamber was maintained to  $\pm 1\%$  RH of the set point in an operational range 5-100% RH. The temperature in the chamber was maintained at  $21\pm 1$  °C. The optical setup for measuring the spectral characteristics of the light diffracted from the hologram was assembled in the environmental chamber. The probe light from a broad band light source (AvaLight-HAL-S, Avantes) was fiber guided into the humidity chamber. The diffracted light was then coupled into a second fiber by a lens and guided to a spectral analyzer (AvaSpec-2048, Avantes). To obtain the

humidity response of a specific grating, the correlation between the peak wavelength of the light diffracted from the nanosteped array and the RH was determined.

### Supporting Information

Atomic Force Microscopy of the honeycomb array with nanosteped pyramids, diffracted light spectra of eight different gratings, diffraction efficiency measurements of the gratings by a powermeter, simulated diffraction spectra of nanosteped pyramids as a refractive index sensor. Supporting Information is available from the Wiley Online Library.

### Acknowledgements

This work is supported by the Leverhulme Trust (RF-2016-039) and the Wellcome Trust (201929/Z/16/Z). We acknowledge James J. Cowan and W. Dennis Slafer for fabricating the Bragg gratings used in this study and discussions on fabrication. We thank Jeff Blyth for discussions. We thank Grant England, Elijah Shirman, Ida Pavlichenko, Joanna Aizenberg, B.V. Lotsch and Viola D. for SEM and AFM imaging.

### Author Contributions

A.K.Y. and A.Y. designed the project. A.K.Y., T.M., and M.H. performed the experiments. H.B., R.A., and Y.M. performed the simulations. A.K.Y. wrote the manuscript. A.Y., H.B., R.A., I.N., and S.M. analyzed the data and edited the manuscript. The authors declare no competing financial interests.

Received: ((will be filled in by the editorial staff))

Revised: ((will be filled in by the editorial staff))

Published online: ((will be filled in by the editorial staff))

[1] J. Ge, Y. Yin, *Angew. Chem., Int. Ed.* 2011, 50, 1492.

[2] D. E. Smalley, Q. Y. J. Smithwick, V. M. Bove, J. Barabas, S. Jolly, *Nature* 2013, 498, 313; C. Fenzl, T. Hirsch, O. S. Wolfbeis, *Angew. Chem., Int. Ed.* 2014, 53, 3318.

- [3] A. Llordés, G. Garcia, J. Gazquez, D. J. Milliron, *Nature* 2013, 500, 323; G. England, M. Kolle, P. Kim, M. Khan, P. Muñoz, E. Mazur, J. Aizenberg, *Proc. Natl. Acad. Sci. U. S. A.* 2014, 111, 15630; M. Schaffner, G. England, M. Kolle, J. Aizenberg, N. Vogel, *Small* 2015, 11, 4334.
- [4] G. Bazin, X. X. Zhu, *Prog. Polym. Sci.* 2013, 38, 406.
- [5] C. I. Aguirre, E. Reguera, A. Stein, *Adv. Funct. Mater.* 2010, 20, 2565.
- [6] F. H. Schacher, P. A. Rugar, I. Manners, *Angew. Chem., Int. Ed.* 2012, 51, 7898.
- [7] D. Schneider, F. Liaqat, E. H. El Boudouti, Y. El Hassouani, B. Djafari-Rouhani, W. Tremel, H.-J. r. Butt, G. Fytas, *Nano Lett.* 2012, 12, 3101.
- [8] J. F. Galisteo-López, M. Ibisate, R. Sapienza, L. S. Froufe-Pérez, Á. Blanco, C. López, *Adv. Mater.* 2011, 23, 30; G. von Freymann, V. Kitaev, B. V. Lotsch, G. A. Ozin, *Chem. Soc. Rev.* 2013, 42, 2528.
- [9] L. Feng, Y.-L. Xu, W. S. Fegadolli, M.-H. Lu, J. E. Oliveira, V. R. Almeida, Y.-F. Chen, A. Scherer, *Nat. Mater.* 2013, 12, 108.
- [10] W. Luo, J. L. Kou, Y. Chen, F. Xu, Y. Q. Lu, *Appl. Phys. Lett.* 2012, 101, 133502.
- [11] S. Takahashi, M. Okano, M. Imada, S. Noda, *Appl. Phys. Lett.* 2006, 89, 123106.
- [12] S. Wong, M. Deubel, F. Pérez - Willard, S. John, G. A. Ozin, M. Wegener, G. von Freymann, *Adv. Mater.* 2006, 18, 265.
- [13] J. Fleming, S. Lin, I. El-Kady, R. Biswas, K. Ho, *Nature* 2002, 417, 52; A. Blanco, E. Chomski, S. Grachtchak, M. Ibisate, S. John, S. W. Leonard, C. Lopez, F. Meseguer, H. Miguez, J. P. Mondia, *Nature* 2000, 405, 437; N. Tétreault, G. von Freymann, M. Deubel, M. Hermatschweiler, F. Perez-Willard, S. John, M. Wegener, G. A. Ozin, *Adv. Mater.* 2006, 18, 457.
- [14] S. Matthias, F. Müller, C. Jamois, R. B. Wehrspohn, U. Gösele, *Adv. Mater.* 2004, 16, 2166.
- [15] G. von Freymann, A. Ledermann, M. Thiel, I. Staude, S. Essig, K. Busch, M. Wegener, *Adv. Funct. Mater.* 2010, 20, 1038.
- [16] P. Viktorovitch, B. Ben Bakir, S. Boutami, J. L. Leclercq, X. Letartre, P. Rojo - Romeo, C. Seassal, M. Zussy, L. Di Cioccio, J. M. Fedeli, *Laser Photon. Rev.* 2010, 4, 401.
- [17] R. Peretti, C. Seassal, P. Viktorovich, X. Letartre, *J. Appl. Phys.* 2014, 116, 023107.
- [18] B. Ben Bakir, C. Seassal, X. Letartre, P. Regreny, M. Gendry, P. Viktorovitch, M. Zussy, L. Di Cioccio, J.-M. Fedeli, *Opt. Express* 2006, 14, 9269.
- [19] Y. N. Denisyuk, *Doklady Akademii Nauk SSSR* 1962, 144, 1275.
- [20] S. A. Benton, V. M. Bove, in *Holographic Imaging*, John Wiley & Sons, Hoboken 2007, 173; B. J. Chang, C. D. Leonard, *Appl. Opt.* 1979, 18, 2407.
- [21] C. P. Tsangarides, A. K. Yetisen, F. D. Vasconcellos, Y. Montelongo, M. M. Qasim, T. D. Wilkinson, C. R. Lowe, H. Butt, *RSC Adv.* 2014, 4, 10454.
- [22] P. N. Tamura, *Appl. Opt.* 1978, 17, 2532; J. L. Walker, S. A. Benton, "In-Situ Swelling for Holographic Color Control", presented at *Practical Holography III*, Los Angeles, CA, 1989.
- [23] E. N. Leith, J. Upatnieks, *J. Opt. Soc. Am.* 1962, 52, 1123.
- [24] S. A. Benton, *U.S. Patent 3,633,989 A*, January 11, 1972.
- [25] J. J. Cowan, *J. Opt. Soc. Am. A* 1990, 7, 1529.
- [26] S. H. Ahn, L. J. Guo, *ACS Nano* 2009, 3, 2304.
- [27] J. J. Cowan, "Advances in holographic replication with the Aztec Structure", presented at *Proceedings of the International Conference on Holography, Wales*, 2006.
- [28] J. J. Cowan, *Opt. Eng.* 1985, 24, 245796; J. J. Cowan, W. Slafer, *Imaging Sci. J.* 1987, 31, 100; M. Ozaki, J.-i. Kato, S. Kawata, *Science* 2011, 332, 218.
- [29] N. S. King, L. Liu, X. Yang, B. Cerjan, H. O. Everitt, P. Nordlander, N. J. Halas, *ACS Nano* 2015, 9, 10628.
- [30] J. Walia, N. Dhindsa, M. Khorasaninejad, S. S. Saini, *Small* 2014, 10, 144.



- [31] Y. Dou, J. Han, T. Wang, M. Wei, D. G. Evans, X. Duan, *J. Mater. Chem.* 2012, 22, 14001.
- [32] P. Aldhous, *Nature* 2005, 434, 132.
- [33] A. K. Yetisen, I. Naydenova, F. da Cruz Vasconcellos, J. Blyth, C. R. Lowe, *Chem. Rev.* 2014, 114, 10654.
- [34] D. Yelin, I. Rizvi, W. M. White, J. T. Motz, T. Hasan, B. E. Bouma, G. J. Tearney, *Nature* 2006, 443, 765.

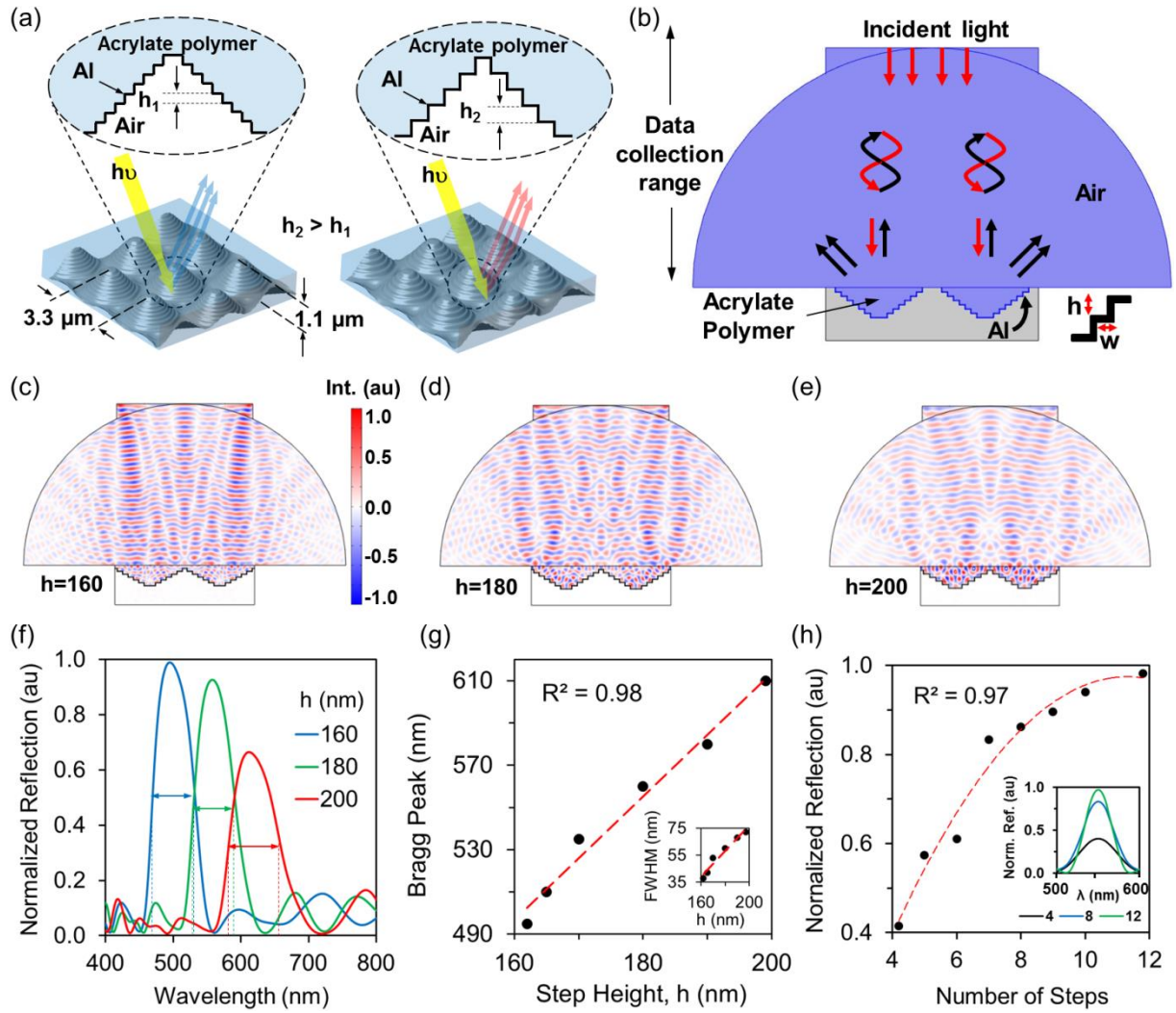


**Figure 1.** Honeycomb array of the circular nanostep pyramids. (a) The principle of operation of the photonic device showing a shift in the diffracted light from blue to red as the step height is increased. (b) Simulated model in a transparent hemisphere screen. Pyramid height was  $1.1 \mu\text{m}$  with a pitch of  $3.3 \mu\text{m}$ , and the overall width and height of the modeled film was  $8$  and  $2 \mu\text{m}$ , respectively. The step width was kept constant at  $250 \text{ nm}$ . Simulated models of the diffracted light at (c)  $496$ , (d)  $558$ , and (e)  $612 \text{ nm}$  show the interaction of the electromagnetic waves with the nanostep pyramids. (f) The positions of the modeled Bragg peaks as a function of the step size at  $160$ ,  $180$ , and  $200 \text{ nm}$ . (g) Bragg peak position with increasing step height. The inset shows broadening FWHM as a function of step height. (h) Reflection as a function of step number. The inset illustrates the diffraction efficiency of pyramids ( $h=180 \text{ nm}$ ) with  $4$ ,  $8$ , and  $12$  steps at  $530 \text{ nm}$ .

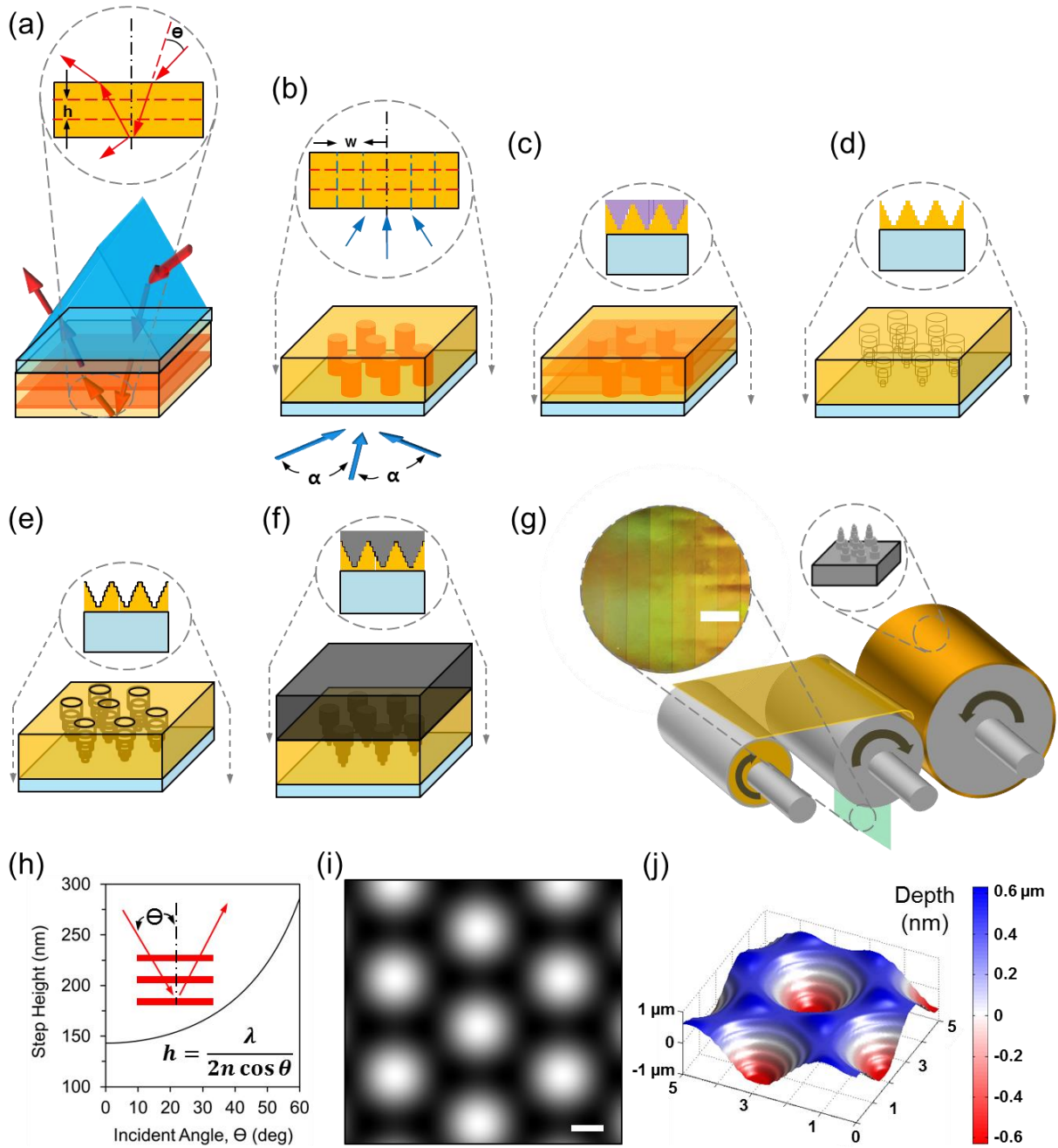


**Figure 2.** Holographic recording and printing of circular nanosteppped pyramids in honeycomb arrays. (a) Prism coupling to expose a multilayer interference in a photoresist layer coated over glass, (b) Laser writing of a honeycomb pattern using three azimuthal beams ( $\alpha=120^\circ$ ) to create a pitch ( $w$ ) of  $3.3 \mu\text{m}$ , (c) Resulting interference, a superposition of the multilayer and the honeycomb pattern, shown in purple (d) Circular nanosteppped pyramids after etching with a photographic developer, (e) Evaporation of a silver layer ( $\sim 300 \text{ nm}$ ) over the etched photoresist in vacuum, (f) Electroplating metallic nickel ( $1 \text{ mm}$ ) over the deposited silver layer to produce a master, (g) Printing the nanosteppped pyramids using a nickel replica into AP on PET film in roll-to-roll manufacturing. The inset shows eight different printed gratings, scale bar =  $4 \text{ cm}$ . (h) The vertical lattice step height of the multilayer as a function of incident angle ( $\theta$ ) in prism coupling, (i) Simulated honeycomb field intensity using three azimuthal beams ( $\alpha=120^\circ$ ) in the photoresist, Scale bar =  $1 \mu\text{m}$ . (j) The modeled nanosteppped concavities computed by superposing the multilayer and the honeycomb exposures.

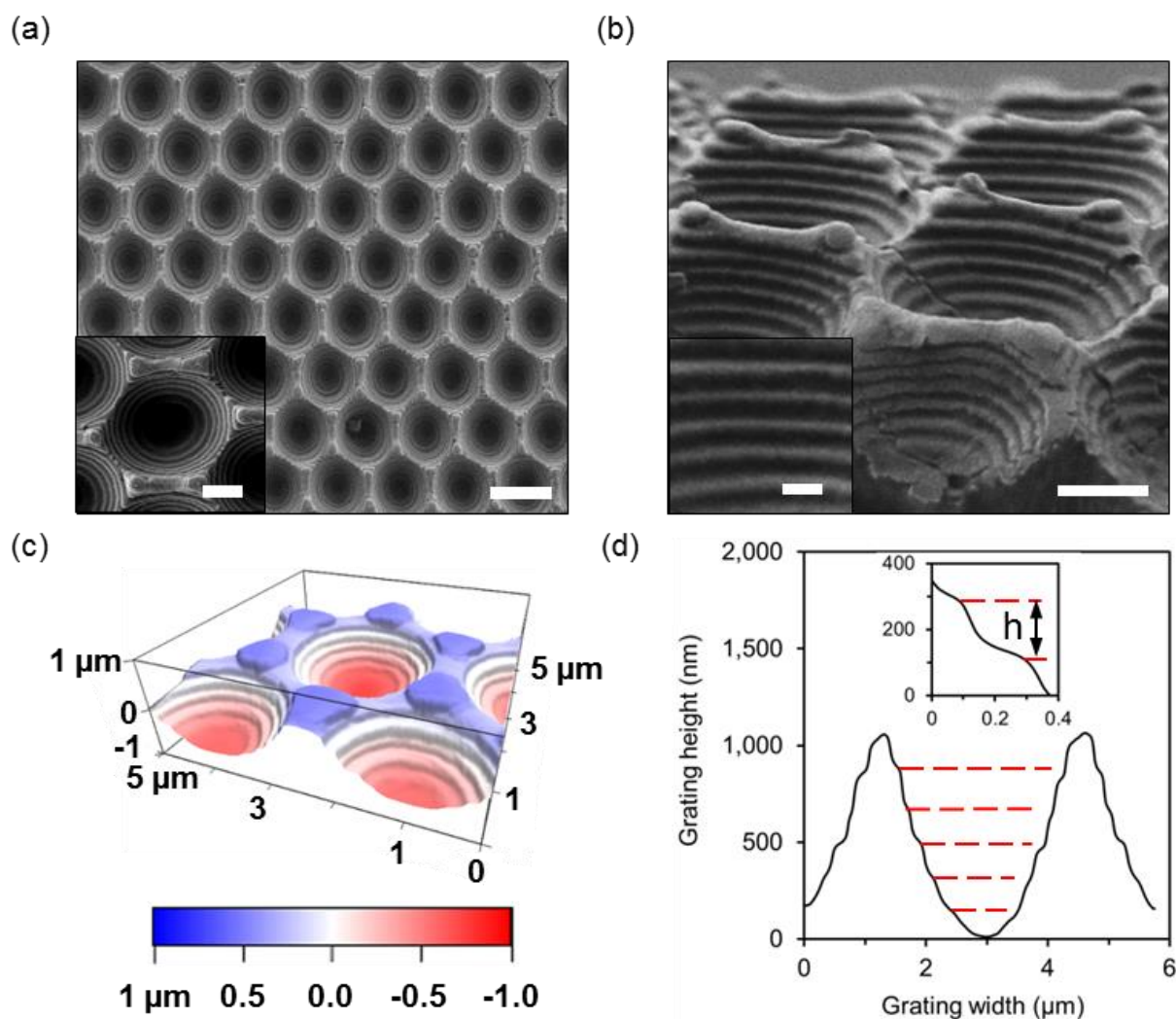


**Figure 3.** Microscopic analyses of the holographic honeycomb array. (a) SEM image of the array shows uniform distribution of circular concavities, Scale bar = 3  $\mu\text{m}$ . The inset shows a single concavity, Inset scale bar = 1  $\mu\text{m}$ , (b) A concavity with 6 steps. Scale bar = 1  $\mu\text{m}$ . The inset shows individual steps. Inset scale bar = 200 nm. (c) AFM surface topography of the array illustrates nanosteped concavities. (d) Measured concavity step height is  $\sim 190$  nm. The inset shows a single step with the width of 200 nm.



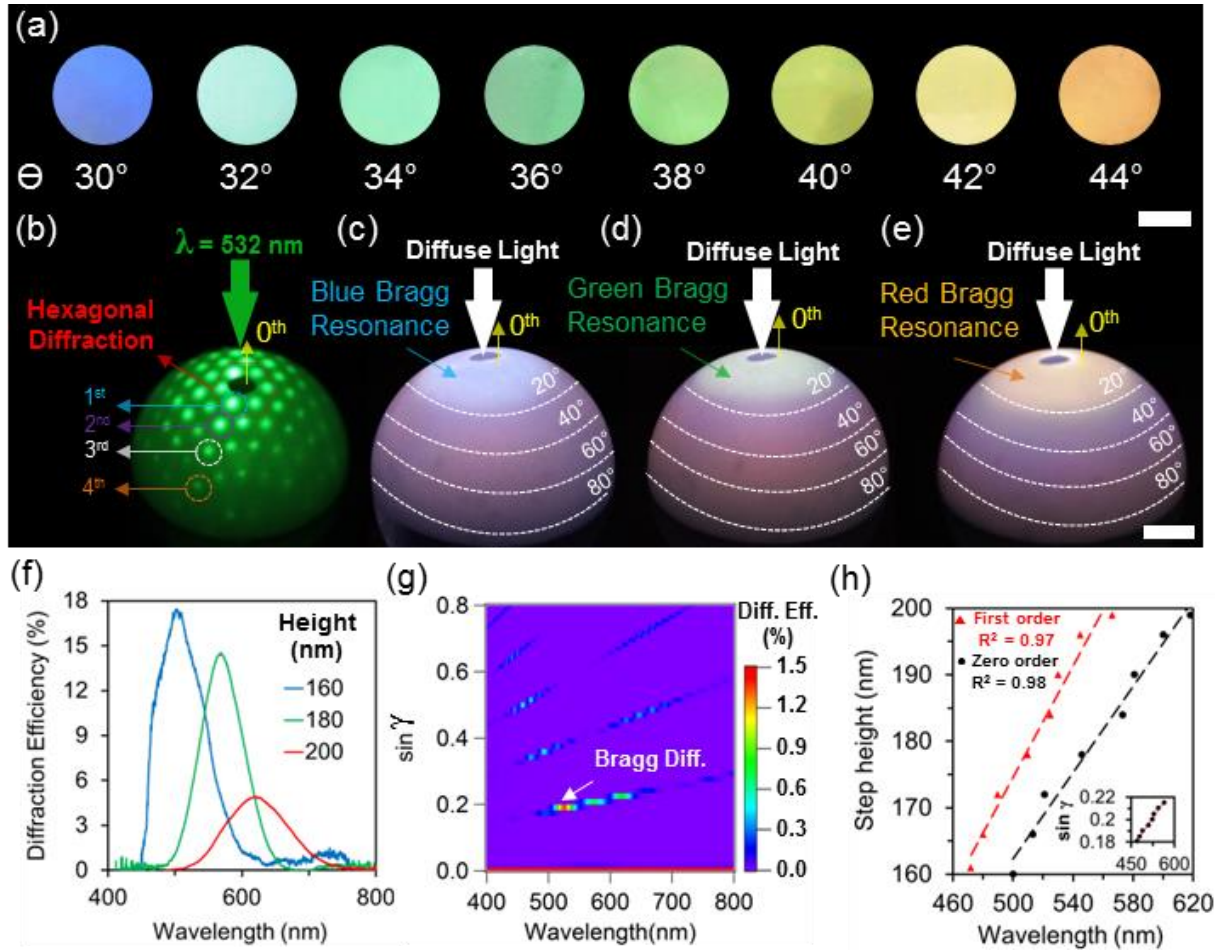


**Figure 4.** Optical characterization of the holographic honeycomb array consisting of nanosteped pyramids. (a) Photographs of eight different gratings produced by increasing the incident angles during prism coupling from  $30^\circ$  to  $44^\circ$ , and subsequent off-axis Leith-Upatnieks patterning. Scale bar = 1 cm. (b) Monochromatic hexagonal light diffraction from a honeycomb array in a hemisphere screen photographed at  $60^\circ$  from the normal. (c) Blue, (d) green, and (e) red resonances of the arrays with step heights of 160, 180, and 200 nm under diffuse light illumination, showing isotropic color distribution below  $20^\circ$  from the normal, photographed at  $80^\circ$  from the normal. The pyramidal array was levelled at the bottom of the hemisphere. (f) Bragg peaks of the nanosteped pyramids ( $h=160-200 \text{ nm}$ ) as a function of step height at normal incidence in the visible spectrum. (g) Angle-resolved spectral measurements of an array with a step height of  $\sim 200 \text{ nm}$ . (h) Zero and first order Bragg peak positions of the nanosteped pyramids as a function of step height. The inset shows angular dependence (160-200 nm).

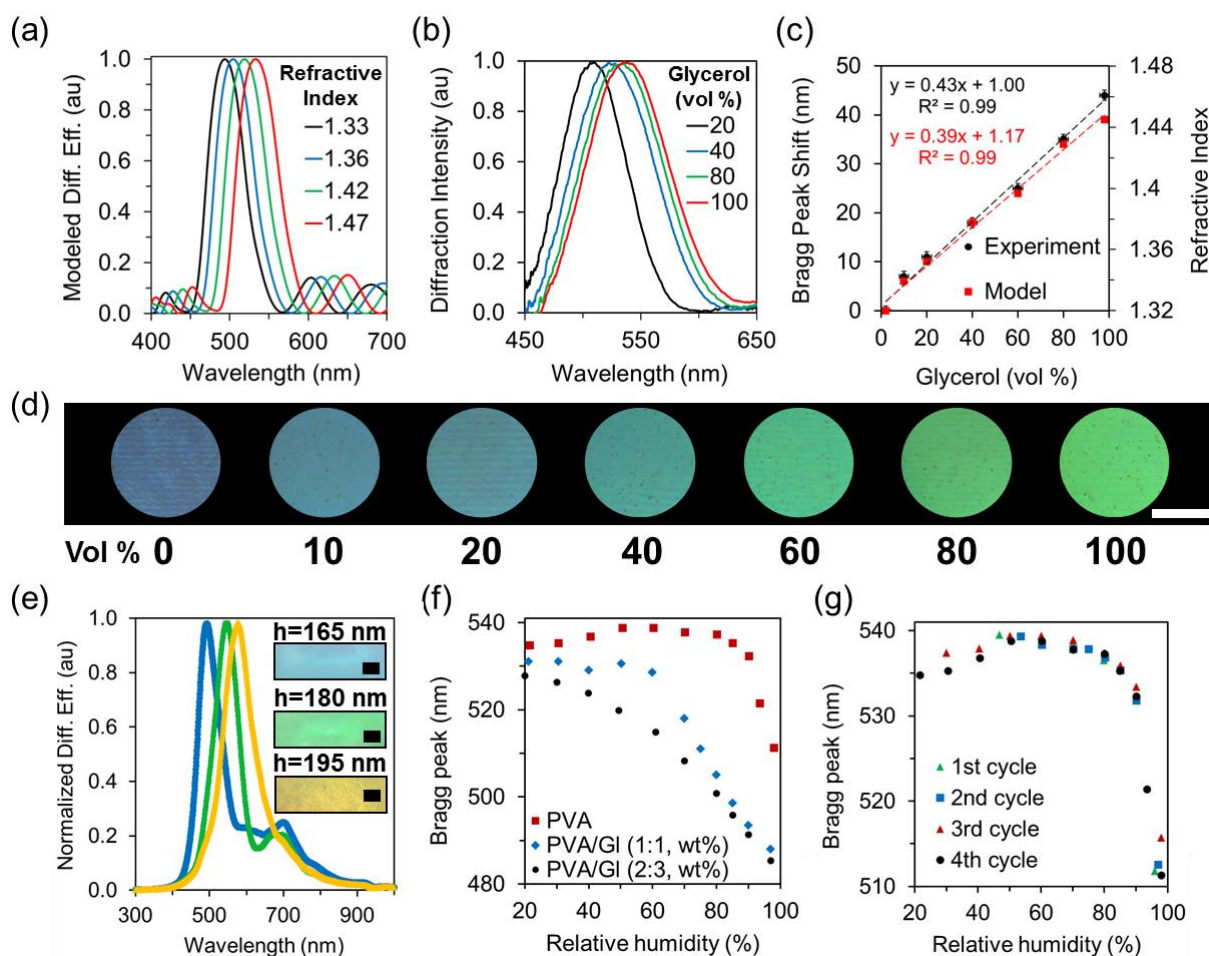


**Figure 5.** The applications of printable holographic nanosteppped Bragg gratings in sensors. (a) Simulated finite element model showing Bragg peak shifts as a function of changes in external refractive index. (b) Nanosteppped pyramid refractive index sensor ( $h=180$  nm), showing 45 nm shift in the position Bragg peak as the concentration of glycerol was increased incrementally. (c) Quantification of the glycerol concentration as a function of variation in refractive index of the surrounding medium ( $n=10$  for each measured sample). (d) The colorimetric readouts of the refractive index sensor with changing glycerol concentration. Scale bar = 5 mm. (e) Bragg peaks of PVA-coated gratings with different nanostep sizes. The inset shows the photographs of the PVA-coated gratings. Scale bar=5 mm. (f) The change in Bragg peak as the humidity increases (g) RH repeat cycles

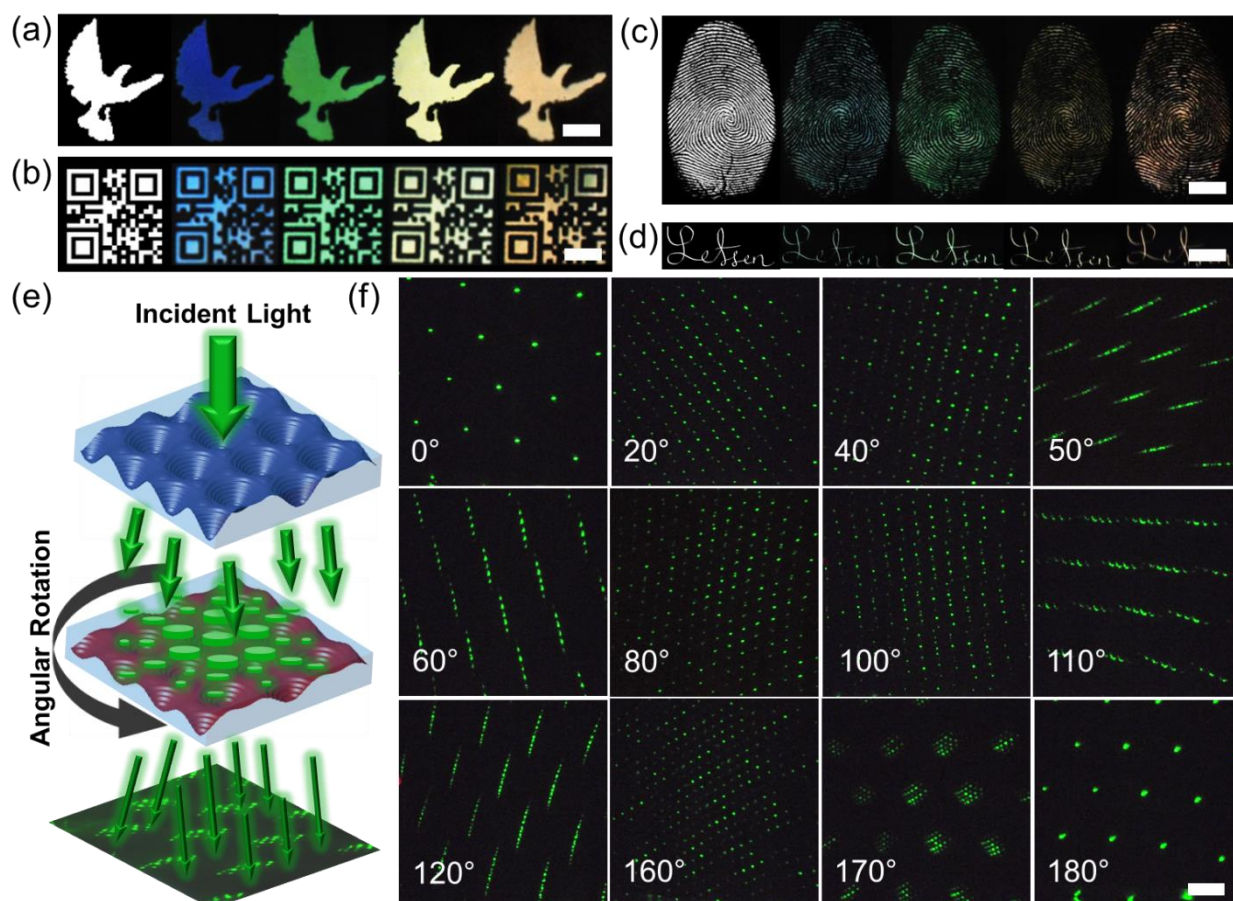


**Figure 6.** The applications of printable holographic nanosteppped Bragg gratings in multilevel security labels. (a) Holographic dove as a security label. The gratings diffract light at 500, 544, 599, and 620 nm, corresponding to step sizes of 160, 180, 195, and 200 nm, photographed from the normal. Left column shows the masks. (b) QR codes, (c) fingerprints, (d) handwritten signatures. Scale bars (a-d)=5 mm. (e) Experimental setup for creating overlapped far-fields using two Bragg gratings in transmission mode (f) Far-field images of nanosteppped Bragg gratings at different angular rotation positions. Scale bar = 2 cm.

**The table of contents entry**

**2.5D nanosteped pyramids** are produced over large flexible substrates using nanoimprinting. The 2.5D structures exhibited a strong coloration due to Bragg diffraction that is tuned in the visible spectrum and a wide angular range. Applications are demonstrated in sensing, holographic images, QR codes, and signatures.

**Keyword: Nanolithography**

A. K. Yetisen,\* H. Butt, T. Mikulchuk, R. Ahmed, Y. Montelongo, M. Humar, N. Jiang, S. Martin, I. Naydenova, S. H. Yun\*

**Color-Selective 2.5 Dimensional Holograms on Large-Area Flexible Substrates for Sensing and Multilevel Security**

ToC figure

